



De-Icing Fluid Flow-Off from a Flat Plate in an Accelerating Airstream

P. Koivisto*

Aalto University, FI-00076 Aalto, Finland

T. Honkanen†

Arteform Ltd., FI-02150 Espoo, Finland

and

M. Auvinen,‡ A. Hellsten,‡ and K. Kahma§

Finnish Meteorological Institute, SF-00101 Helsinki, Finland

<https://doi.org/10.2514/1.J058706>

De-icing fluid flow-off from a flat plate subjected to an accelerating airflow was studied both experimentally and using computational fluid dynamics (CFD) simulations. The experimental tests were carried out in Aalto University's 2 m × 2 m Low Speed Wind Tunnel using two different flat plate models, with chords of 0.6 and 1.8 m. The OpenFOAM software library was used in the CFD simulation for the 0.6 m flat plate model. Both measurements and CFD simulations supported the assumption that the solitary waves dominating the flow-off process were kinematic, mass transporting, in nature. For the first 50% of the fluid thickness decrease, the wave speeds and the mean fluid flow speed are almost linearly dependent on the wind tunnel speed on both flat plate models. The fluid thickness at the end of simulation predicted well the measured value.

Nomenclature

a	=	wave amplitude
c_w	=	wave speed
h	=	fluid thickness
I	=	intensity of transmitted light
I_0	=	intensity of incident light
k	=	turbulence kinetic energy
k_w	=	wave number ($1/\lambda$)
L	=	flat plate chord
Re_G	=	gas Re number
Re_L	=	liquid Re number
S	=	wave separation (solitary wave)
U	=	wind tunnel speed
\bar{u}	=	2D mean fluid speed
\bar{u}_i	=	resolved velocity components (i is equal to 1, 2, 3)
V	=	speed vector (u, v, w)
v_i	=	local velocity component (i is equal to 1, 2, 3)
$y+$	=	nondimensional wall distance (u^*y/ν , where u^* is friction velocity)
Δ	=	filter width
Δh	=	fluid thickness increment in time step Δt
Δt	=	time step
ϵ	=	light absorption coefficient
λ	=	wavelength (periodic wave)

I. Introduction

ANTI-ICING treatment protects the wing of an airplane before the takeoff from precipitation-induced contamination (snow,

Received 5 June 2019; revision received 30 October 2019; accepted for publication 23 November 2019; published online 18 December 2019. Copyright © 2019 by Pekka Koivisto. Published by the American Institute of Aeronautics and Astronautics, Inc., with permission. All requests for copying and permission to reprint should be submitted to CCC at www.copyright.com; employ the eISSN 1533-385X to initiate your request. See also AIAA Rights and Permissions www.aiaa.org/randp.

*Doctoral Student, Department of Mechanical Engineering, Sähkömekaninen 4.

†Research Engineer, Teollisuustie 7 C 1, 02880, Veikkola.

‡Senior Research Scientist, Atmospheric Dispersion Modelling, P.O. Box 503, Erik Palménin aukio 1.

§Research Professor, Marine Research Programme, P.O. Box 503, Erik Palménin aukio 1.

ice, frost). Anti-icing fluids are mostly glycol-based fluids designed to flow-off from the wing surface during the takeoff run to ensure adequate aerodynamic performance after liftoff. As thickened anti-icing fluids (types II, III, and IV) are non-Newtonian shear thinning fluids, they should persist on the wing and absorb precipitation during taxi but leave the wing more easily during the takeoff run. In a shear thinning fluid, the viscosity drops to a fraction of its initial value when shear forces of the air stream affect the fluid surface. The decreasing viscosity improves the fluid flow-off during the takeoff run.

De-icing fluids (type I), studied in the present paper, are not designed to absorb precipitation or to persist on the wing surface during taxiing. They are Newtonian fluids with viscosities not depending on the shear stress. The viscosities of de-icing fluids are considerably lower than the viscosities of the thickened anti-icing fluids, which means that their flow-off from the wing surface normally generates less aerodynamic penalties. In practice anti-icing treatment never leads to a completely aerodynamically clean surface, which causes some lift degradation during takeoff. This also applies, to some extent, to the de-icing fluids especially at subfreezing temperatures. Whatever type of fluid is applied on the wing before the takeoff, the fluid elimination from the surface should be complete enough to leave an aerodynamically acceptable wing surface.

The beginning of scientific research focusing on the de/anti-icing fluid behavior and aerodynamic effects can be dated back to the late 1980s and early 1990s. In most of these early studies the main objective was to establish a scientific basis for an aerodynamic acceptance test (AAT) [1] for the fluids. The most significant research work performed to establish an acceptance test was carried out by Boeing [2,3], NASA Lewis Research Center [4], and Von Karman Institute for Fluid Dynamics [5–8]. In the AAT the tested fluid is applied on a flat plate, which is then subjected to an accelerating airflow in a wind tunnel to simulate the conditions on an aircraft wing during the takeoff run. During the wind tunnel test, the boundary-layer displacement thickness (BLDT) growth caused by the fluid is determined at the trailing edge area by comparing the pressure difference values within the test section. To pass the test, the BLDT growth due to the fluid tested at the end of airflow acceleration shall be under the acceptance limit defined by the industry. For all fluids there are also requirements for the remaining fluid after the test. For type I it is the maximum remaining thickness, and for types II, III, and IV it is the elimination percentages.

The above-mentioned research focused mainly on the assessment of aerodynamic disadvantages caused by the fluid at the point of aircraft liftoff or during initial climb and less on the question of fluid

flow-off properties when subjected to an airflow. However, the general problem of the behavior of a free liquid surface subjected to an airflow is much older. The first attempt to explain the wind-wave formation was proposed by Helmholtz and Kelvin [9,10], and the Kelvin–Helmholtz instability is now a paradigm for instabilities in fluid mechanics. Among the large body of literature on the subject, pioneering theoretical contributions in this field are those of Phillips [11] and Miles [12]. The early work on wind waves considered mostly deep-water waves. Cohen and Hanratty [13] and Craik [14] used Orr–Sommerfeld stability analyses for horizontal liquid films sheared by turbulent gas flows to predict conditions under which waves appear and the factors controlling their growth. Cohen and Hanratty [13] found that quantitative predictions of the speeds and wavelengths of the fastest growing waves were reasonably accurate when the gas flow was modeled using the Orr–Sommerfeld solutions (which neglected turbulence) given by Miles [12].

Since late 1980s a growing number of theoretical investigations were published considering de/anti-icing fluid wave formation when subjected to an airflow. The general interest in the stability of liquid films in an air flow has increased the understanding of de/anti-icing fluid behavior too. Yih [15] was perhaps the first to focus specifically on the de-icing fluids in his study. His paper was a stability analysis based on Orr–Sommerfeld equations. After Yih's study there was a steady flow of papers throughout the 1990s. References [16–20] represent a typical part of those studies. The main interest in this research was then the linear stability theory which is based either on Orr–Sommerfeld equations [17,20], asymptotic expansions [18] or parabolized stability equations (PSE) [19].

A shortcoming of the linear stability analysis is that it covers only the periodic wave phenomena. The periodic waves on the surface of de-icing fluids occur on a wing surface only for a very limited period during the air flow acceleration when the aircraft takeoff conditions are considered. For non-Newtonian fluids (types II, III, and IV) this phase is mostly nonexistent as discovered by Carbonaro and Özgen [21] and Cunha and Carbonaro [22]. In an accelerated airflow, where the periodic fluid waves are initially present (in airflows over Newtonian fluids), they are followed by nonperiodic solitary waves. According to Cunha and Carbonaro [22] and Özgen et al. [23] solitary waves considerably enhance the transportation of fluid. Jurman and McCready [24] and Peng et al. [25] point out in their work that it is the solitary waves that are responsible for fluid transfer. In considering de/anti-icing fluids, which should flow well off the wing surface before the aircraft lift off, the formation and development of solitary waves are then essential.

Compared with the number of studies focusing on the linear stability considerations in liquid film subjected to airflow, the research focused on the solitary wave phenomena is quite limited. Jurman and McCready [24] and Peng et al. [25] have studied both theoretically and experimentally the gas sheared liquid film wave formation. The liquid used in their study was diluted glycerine. Diluted glycerine has higher viscosity values compared with the commonly used water. According to Jurman and McCready, sufficiently high liquid viscosity reveals the regions where steady waveforms of different types exist. Based on experiments, Peng et al. [25] created a clear wave regime map for gas sheared liquid layers and distinguished the characteristics of periodic and solitary wave formation clearly from each other. Jurman and McCready [24] introduce in their theoretical analysis a two-wave structure, revealing the presence of both kinematic and dynamic waves, which occur simultaneously. The kinematic waves are, according to Jurman and McCready [24], responsible for transporting fluid. They are of special interest in the present study and will be considered in closer detail in this paper. Among the scarce amount of research considering solitary waves, the study of Vlachomitrou and Pelekasis [26] should be noted. They examine the formation of solitary waves theoretically using the triple-deck theory.

The more recent research on liquid films subjected to an airflow is water related [27–29]. Water, however, due to its much lower viscosity behaves clearly differently compared with the de/anti-icing fluids. Leng et al. [27] consider the interesting question of airflow-related water film transfer. Although they briefly describe the wave phenomena on the liquid surface, they assume the liquid transfer to be skin

friction related, omitting the role of surface waves in the process. In their second study [28], Leng et al. give a more extensive description of the wave phenomena; however, they end up explaining the liquid transfer using a semi-empirical formula for friction coefficient as in [27]. Sakakeeny et al. [29] have investigated the water film behavior on a NACA 0012 wing section surface subjected to airflow of inlet speeds from 1 to 10 m/s using both 2D and 3D direct numerical simulation (DNS). As the DNS is still a computing-time-limited method, a 2D model for higher inlet speeds is used. The simulation time in [29] is nevertheless limited to quarter of a second. However, they clearly catch initial wave phenomena on the water surface in 2D simulation and the beginning of turbulence onset in three dimensions.

Considering the de/anti-icing fluid behavior on the wing surface during the takeoff run, the most relevant feature is the quantitative reduction of the fluid film over time. The research referred to above has not addressed this problem directly. Considering the phenomenon of de/anti-icing fluid flow-off from an aircraft wing during takeoff, the published literature referred to above suffers from the following deficiencies:

- 1) Detailed information on growth factor variation with wave number included in stability analysis does not enhance understanding on fluid mass transfer related to the airflow-induced fluid wave motion.
- 2) Test arrangements often incorporate arrangements to maintain a steady constant airflow and an adjustable constant fluid thickness in the test section with an adjusted continuous fluid flow; this arrangement prevents the detection of fluid flow-off during an accelerated airflow, which is the situation to be simulated, for example, in the de/anti-icing fluid AATs.

- 3) Most of the test sections are very small; the dimensions in the test section imply a wall boundary-layer-disturbed air flow—often a fully developed 3D profiled flow—not simulating properly the flow over an aircraft wing.

Presently, the only generally applied method to assess the de/anti-icing fluid flow-off qualities is the AAT in an authorized wind tunnel. Especially for fluid manufacturers, however, a feasible computational method would be very valuable in their fluid development projects. The general problem of liquid fluid film flow-off in a gas stream is naturally not restricted to airplane de/anti-icing applications only.

II. Objectives

The main objective of this study is to improve the understanding of the type I Newtonian de-icing fluid flow-off mechanics when subjected to an accelerated airflow. The previous research has concentrated mostly on the stability and wave onset issues of a liquid film in a gas stream. The present study is focusing on the fluid flow-off process instead and particularly on the role of kinematic waves introduced by Jurman and McCready [24].

As was noticed earlier, most of the experimental studies referred to above have been performed in channels with dimensions that do not enable a flow free of wall effects to simulate the conditions on an aircraft wing during the takeoff. Even the de/anti-icing fluid AAT wind tunnel is specified to be quite small in dimensions. The test section dimensions are approximately 300 mm wide and 100 mm high with a length of 1.5 m. The measurements in this study are performed in a wind tunnel planned for aircraft models, which makes possible an airflow practically free of wall effects. The comparison of the wave formation and geometric properties (amplitude and wave separation) and wave speeds measured with earlier experimental results is considered as an objective too.

The authors are not aware of any studies published using computational fluid dynamics (CFD) tools in simulating the liquid film layer flow-off phenomena in an accelerated airflow. One of the objectives is to assess the utility of an open source software library (OpenFOAM) for this purpose. The fluid layer considered is a Newtonian type I de-icing fluid as a first step to avoid the problems raised by the time-dependent material properties of the non-Newtonian anti-icing fluids. The CFD tools are used specifically to have a better insight into the liquid layer fluid dynamics during the de-icing fluid flow-off.

III. Experiments

A. Wind Tunnel and Models

Aalto University's Low Speed Wind Tunnel is a closed-circuit wind tunnel with test section dimensions of 2 m × 2 m and test section length of 4 m. The flow nonuniformity in the test section is <3.4%, and turbulence level <0.28% at the wind tunnel speed of 60 m/s. As the fluid flow-off was measured during an accelerating airflow simulating an airplane takeoff run, the turbulence intensity of the wind tunnel was also determined during the acceleration. The maximum peak value of the turbulence level occurred at the very beginning of the acceleration period and was less than 0.6%.

The wind tunnel tests were done using two different flat plate models with chords of 0.6 and 1.8 m and span of 0.3 m. These dimensions were selected to ensure the maximum available scale effect between the two plates. The flat plate models were adjusted to the wind tunnel as described in Fig. 1. The plate distance from the test section floor level was 0.4 m, and the height of the light source unit 0.05 m. The possible pressure variation inside the structure supporting the plate is relieved by holes in the vertical supporting plates. This arrangement gives a properly 2D and wall-effect free flow over the flat plate. The flow conditions in the wind tunnel tests of the present study adequately simulate the conditions on a wing surface, because the wind tunnel wall boundary layers do not disturb the air flow over the fluid layer.

B. Measurements

To simulate a de-iced wing during the takeoff run, the flat plate has been applied with a layer of fluid before the test run. The initial thicknesses for the tests were as follows:

- 1) 0.6 m model: 1.1, 1.2, and 1.3 mm
- 2) 1.8 m model: 1.5, 1.9, and 2.1 mm

As the extra fluid runoff was not prevented during the fluid application, the attainable maximum initial thickness of the applied fluid layer for a specific fluid depends on the dimensions of the plate. The thicknesses of 1.3 mm (0.6 m plate) and 2.1 mm (1.8 m plate) were the maximum attainable thicknesses with the fluid used.

During the tests, airflow acceleration followed approximately the AAT sequence defined in SAE AS 5900 [1]. The adopted accelerating speed sequence in the wind tunnel tests is described in Fig. 2. The SAE AS 5900 maximum speed of 65 m/s and acceleration of 2.6 m/s² were not acceptable due to practical limitations of the wind tunnel fan motor. The maximum speed was limited to 60 m/s and acceleration to 2.0 m/s². Wind tunnel idle speed was 5 m/s, which is a widely accepted idle speed.

The measuring of the fluid thickness during a test run in the present study follows the light absorption technique, which correlates the thickness of the fluid to the transmitted light intensity. This method was applied also by Özgen et al. [23] and Craik et al. [30]. Considering a medium in an incident light, only a part of its intensity is transmitted to the other side. In other words, there is a loss of intensity

due to reflection ("spurious effect") and absorption ("useful effect"). An observer positioned above the medium would see an intensity inversely proportional to the length of the path followed by the light inside the medium. The relation between the incident light and the transmitted light is given by

$$I = I_0 \{ \exp(-\epsilon h) \} \quad (1)$$

in which I_0 is the incident light intensity, I the transmitted light intensity, ϵ the light absorption coefficient, and h the medium thickness. Knowing ϵ from a suitable calibration it is possible to obtain the medium thickness by measuring the transmitted intensity.

Below the flat plate model there was a light source consisting of 240 white LEDs with color temperatures of 6000–7000 K with a total power of 320 W. The light goes through a transparent Plexiglas flat plate model, and this light was recorded by a video camera on the top of the test section (Fig. 3). The type I fluid used was originally a colorless special batch from the fluid manufacturer, and it was dyed with a sufficient amount of green dye. The extra amount of color

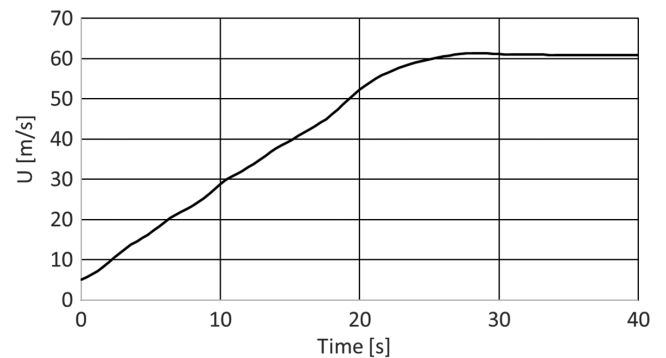


Fig. 2 Wind tunnel speed acceleration sequence used in the present study.

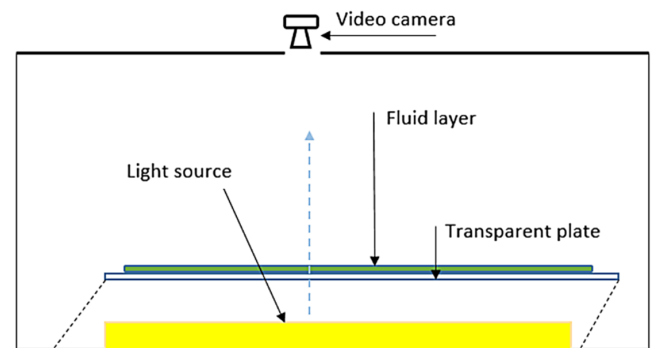


Fig. 3 Flat plate model in the wind tunnel test section.

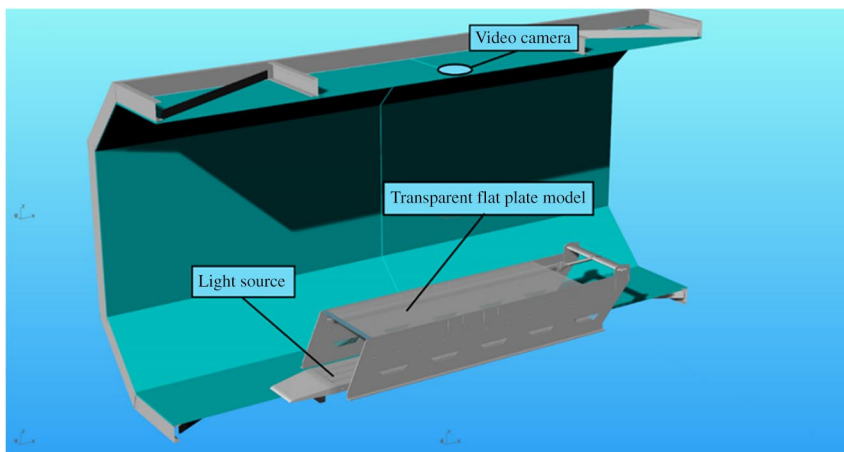


Fig. 1 Flat plate wind tunnel model arrangements in the test section.

pigment gave better image contrast without using any filters in the camera objective.

The light intensity was calculated out of video frame pixel RGB values. The calibration was carried out using a wedge-shaped Plexiglas container filled to predetermined amount of fluid. To avoid the surface tension effect cambering the fluid surface at fluid–container interface, a Plexiglas sheet was adjusted above the fluid surface to force the fluid thickness to grow linearly from zero thickness to maximum thickness of 7 mm. This improved the calibration accuracy especially at the important low end of thicknesses (below 2 mm). The calibration curve was produced using two takes: one without the fluid in the wedge container and the other with a fluid filled container. Subtracting the pixel intensities of these two gives the absorption levels of the fluid with different thicknesses. Calibration curve followed the shape determined by Eq. (1). The calibration curve from 0 to 7 mm corresponded relative pixel intensity levels from 0 to 120. In addition to the calibration procedure, the stationary fluid layer after fluid application over the flat plate model before starting the wind tunnel was both video filmed and measured manually with a fluid thickness gauge to assess the accuracy of the calibration for each run. This procedure was followed also after the wind tunnel run to assess the measurement accuracy of the very low thickness values (0.05–0.2 mm).

There were two different video cameras used for recordings. Both cameras had a field of view covering the whole plate (1800 mm × 300 mm) with a stationary camera. Both cameras gave a spatial resolution of 0.98 mm per pixel. The frame rate of the video camera used for the 0.6 m model was 25 frames/s and of the one used for the 1.8 m model 50 frames/s. The fluid thickness values were calculated from the subtraction of the RGB values of a video frame of the model without fluid and the RGB values of a frame with fluid on the plate using the calibration curves. The mean thickness of the fluid over the plate was integrated from the measured values over the whole plate.

Comparison between the stationary fluid thickness recordings and manually measured thicknesses gave very different results for the two different models. The difference in mean thicknesses was from 0.15 to 0.2 mm for the 1.8 m model, whereas it was from 0.01 to 0.05 mm for the 0.6 m model. The reason for this difference may partly be due to the two different video cameras used for different models. Also, the calibrations were individual for each video run which, may explain the difference. As there was a general noise level of about 0.2 mm in the video recordings, the absolute accuracy was not even close to the

above-mentioned differences in stationary mean thickness values. However, the integrated video-frame-calculated mean thicknesses proved to be close to the manually measured values. The manual measurements were done with a thickness gauge. The pointwise fluid thickness values measured varied from 0.9 to 2.2 mm, which means a measurement resolution of no better than 0.05–0.2 mm depending on thickness value measured.

The analysis of wave characteristics was in focus in the present study. The most critical accuracy factor influencing this may be considered the relatively high noise level of 0.2 mm. This made it impossible to observe waves at fluid layers thinner than 0.2 mm. However, the most important wave phenomena were easily detected as consisting significantly larger waves. The noise level did not affect the integrated mean fluid thickness, which played an important role in results.

C. Experimental Results

1. Wave Onset and General Observations

The events on the fluid surface follow the same general pattern for both plates (0.6 and 1.8 m). The fluid layer is flat until the wave onset air speed, which varies between 9 and 10 m/s for both models. There is no correlation between fluid initial thickness and wave onset speed for fluid thicknesses between 1.1 and 2.1 mm. The first waves appearing are clearly regular and periodic. The wavy area covers first a limited area of the plate and progresses over the whole plate within approximately 1 s. As the air speed further increases, solitary waves appear to the leading-edge area of the plate. Figure 4 illustrates the situation for a 1.8 m plate as the periodic waves cover almost the entire plate and the first solitary waves are appearing on the leading-edge area. In Fig. 5 solitary waves have taken over to cover the whole plate. The wave pattern is not as regular as in Fig. 4, and the wave speeds are clearly higher. There is no clear wavelength, and the separation between waves is larger. The colors have been manipulated with an image manipulation software in Figs. 4 and 5.

Figures 6 and 7 illustrate the measured wave forms of periodic and solitary waves graphically for the 0.6 m flat plate. The wavelength λ for periodic waves and the wave separation S for solitary waves are defined in Figs. 6 and 7. The initial fluid thickness in Figs. 4 and 5 was 1.5 mm, and in Figs. 6 and 7 it was 1.3 mm.

Özgen et al. [23] studied the critical (wave onset) wind tunnel speed and characteristics of the periodic waves in VKI CWT-1 wind

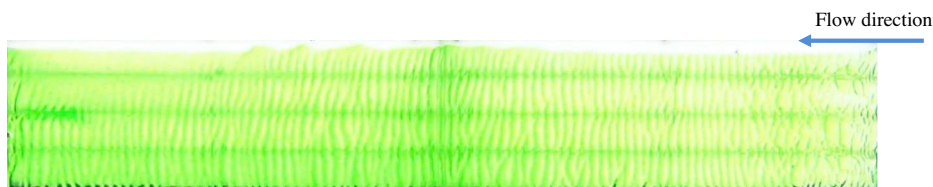


Fig. 4 Initial periodic waves at wind tunnel speed of 12.2 m/s for an initial thickness of 1.5 mm.

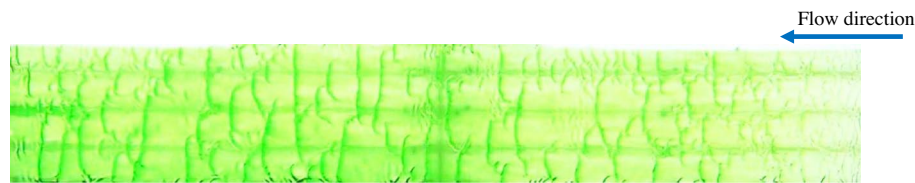


Fig. 5 Solitary wave pattern at wind tunnel speed of 15.6 m/s for an initial thickness of 1.5 mm.

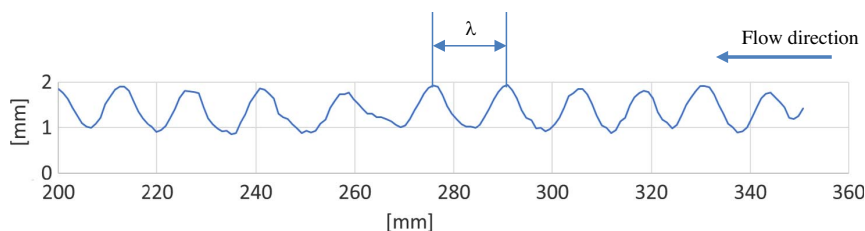


Fig. 6 Measured periodic waves for an initial thickness of 1.3 mm. Wavelength = λ .

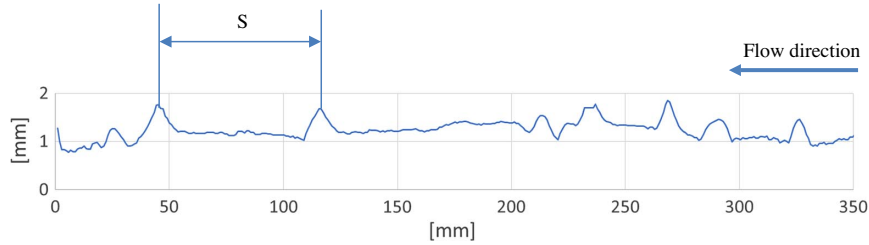


Fig. 7 Measured solitary waves for an initial thickness of 1.3 mm. Wave separation = S .

tunnel using a de-icing fluid with material properties almost the same as in the present study. The results of Özgen et al. and the present study (with the 1.8 m plate) have been collected in Table 1. As the results of Table 1 are dependent on fluid initial thickness, a straightforward comparison between the present study and [24] is not possible. However, if the results are considered as functions of initial fluid thicknesses, U_{cr} may be estimated to deviate about 10% and λ about 28% from the pattern of results in [24], whereas c_w is well on the linear pattern of the results in [24]. Note that the VKI CWT-1 wind tunnel test section dimensions are 300 mm wide and 100 mm high with a length of 1.5 m, which makes it more like a channel compared with the test section of the present study wind tunnel with dimensions an order of a magnitude larger.

Özgen et al. [23] devote a considerable portion of their study to a numerical solution of Orr–Sommerfeld equation, which leads to results close to their experimental results. This strongly suggests that both the initial type I fluid periodic waves observed in the present study and the waves observed in Ref. [23] are in accordance with waves predicted by the linear stability theory.

Cunha and Carbonaro [22] present the wave number variation with the fluid initial thickness for periodic waves. Their measurements were also conducted in the VKI CWT-1 wind tunnel discussed above. These results are compared with the present study results in Fig. 8, where the variation of the wave number k_w (the inverse of wavelength) with fluid initial thickness is illustrated. The exact material constants of the de-icing fluid and test conditions of [22] are unknown. The results of these two studies seem to be consistent.

As the airspeed is increased, the periodic linear waves are replaced by solitary waves. The wave pattern becomes more irregular, and the waves seem to be more or less individual in nature though they appear in frequent lines. Another feature of the solitary waves is that they appear and disappear along the plate and merge with each other in a random sequence. Note that the wind tunnel speed in the study of Özgen et al. [23] was never increased above the speed where the initial periodic waves appeared. This may be the reason why Ref. [23] does not mention this transition from periodic waves to solitary waves.

2. Kinematic and Dynamic Waves

Jurman and McCready [24] consider in their study the waves on thin liquid films sheared by turbulent gas flows. The test arrangements they are referring to include a rectangular air channel 300 mm wide, 25.4 mm high, and 9 m long with a liquid covered floor. The liquid they used was a glycerine–water solution. The liquid was circulated by pumping it within a separate circuit with an adjustable constant-volume flow. Also, the airspeed in the channel was constant through each separate test.

Although their test arrangements are quite different from the ones in the present study, where the airflow is accelerated in a wider wind tunnel and the fluid is permanently sheared off from the test plate, the results of Jurman and McCready’s study are into some extent applicable. Especially the wave behavior map they introduce seems to be consistent with observations made in the present study. In the wave map presented in Fig. 9 the type of waves observed in the tests has been plotted to a parameter space of air (gas) and liquid Re numbers. The liquid they use is a glycerin–water solution with a dynamic viscosity of 14–20 mPa · s. The air Re number (Re_G) is referred to the height of the channel, which in their study is only 25.4 mm. As the wind tunnel height in the present study is two orders of magnitude larger, Re_G defined as in [24] is not a reasonable parameter to compare. The air stream in the test channel considered in Jurman and McCready study is practically a fully developed boundary-layer flow, which is in stark contradiction to the airflow in the present study. However, to get an impression on the airflow in Fig. 9 Re_G of 10,000 corresponds mean air speed of 5.9 m/s in the test channel of [24]. The liquid Re number (Re_L) in Fig. 9 is referred to as the mean fluid thickness.

To orientate the present study’s fluid behavior on the wave map of Fig. 9, the de-icing fluid Re number variation during the acceleration tests was calculated using the mean volume flow and mean thickness value on the flat plate. The de-icing fluid Re number referred to fluid’s mean thickness varies between 0 and 3 for both plates during the acceleration tests.

Drawing a vertical line at $Re_L = 3$ on the wave map figure of Fig. 9 shows, according to Jurman and McCready, that as the air speed (Re_G) is increased, the first waves are 2D periodic waves. As the limiting curves for 3D periodic waves and solitary waves merge at the lowest Re_L numbers, it seems apparent that 2D periodic waves will turn to solitary waves directly without the intermediate 3D periodic phase. According to the observations (see Figs. 4 and 5) this is the sequence of events in the present study for both plates.

In their theoretical analysis Jurman and McCready [24] end up dividing the wave formations into two wave types:

1) Kinematic waves with an approximate characteristic velocity equal to about twice the average film velocity. This wave is only weakly dispersive and is expected to be a low-frequency disturbance. These waves transport fluid, a property that follows directly from continuity (Lighthill and Whitham [31]).

2) Dynamic or “inertial” waves. This wave is dispersive; its speed is largely governed by fluid inertia, gravity, and surface tension. No net transport of fluid is associated with the motion of this wave type.

The main objective of the present study (Sec. II) is to gain better understanding on the flow-off process of the de-icing fluid when subjected to an accelerated airflow. The division of wave formations to kinematic and dynamic wave types defines the waves’ ability to

Table 1 Initial wave characteristics in a constant-airspeed test of Ref. [23] and the present study for type I fluid

Study	\bar{h} , mm	U_{cr} , m/s	λ , mm	c_w , mm/s	ρ_{fluid} , kg/m ³	σ , N/m	μ , cP · s
Ref. [23] (1.5 m plate)	2.3	10.7	22.1	99.4	1030	0.036	37
	1.9	10.8	22.6	81.3	1030	0.036	37
	1.0	11.0	28.8	9.1	1030	0.036	37
Present study (1.8 m plate)	1.5	9.7	18.4	68.2	1040	0.036	50

Note: \bar{h} = fluid mean thickness; U_{cr} = wave onset wind tunnel speed; λ = wave length; c_w = wave speed; ρ_{fluid} = fluid density; σ = surface tension between air and fluid; μ = fluid dynamic viscosity.

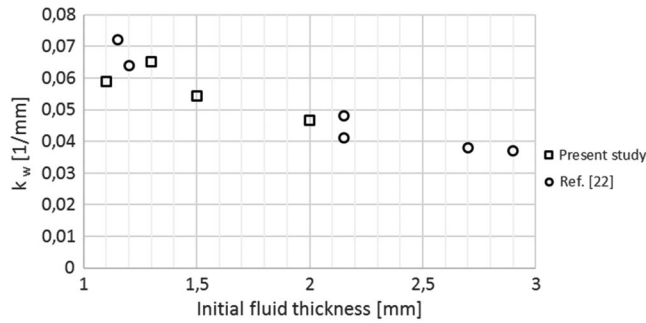


Fig. 8 Wave number k_w variation with fluid initial thickness for periodic waves.

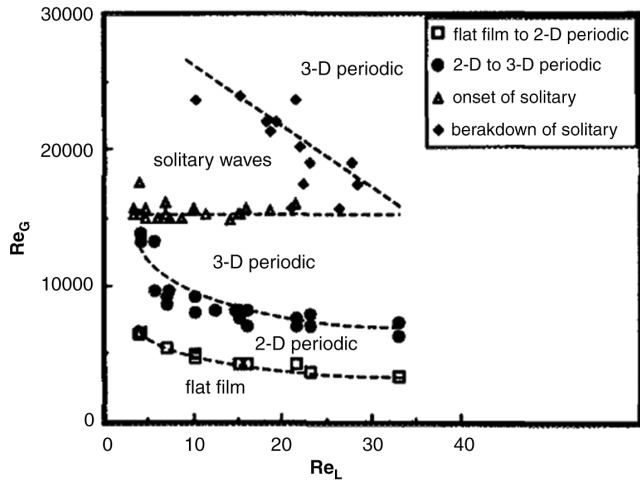


Fig. 9 Wave map in Re_L – Re_G parameter space. The figure is copied from Jurman and McCready's study [24].

transfer the fluid. Quoting Jurman and McCready: “It is important to note that solitary waves, which occur on viscous fluids if Re_G is greater than about 15000, are clearly kinematic in nature because they carry significant fluid as they travel. The two-dimensional waves that form initially from a flat film of . . . are primarily of a dynamic nature over essentially the entire range of Fig. 5” (Fig. 9 in this paper).

Figure 10 illustrates the wave formation on the 0.6 m plate of the present study at a wind tunnel speed of 14.3 m/s and initial fluid thickness of 1.3 mm. At the right end of the figure the waves are clearly periodic. Wave formation is shifting toward solitary ones in the flow direction. There is a 0.04 s time shift between the red and blue curves. As the time resolution between two frames is 40 ms, this is the shortest interval to be detected for the 0.6 m plate. Figure 10 shows how the wave speed increases when waves transform from periodic to solitary ones. According to Jurman and McCready [24] the transfer of fluid also increases accordingly. In their theoretical analysis, they arrive at a simple relationship between the average liquid film speed and the solitary—or kinematic—wave speed. The approximate kinematic wave speed is shown in their paper to be two times the average liquid film speed. Although being a theoretical simplification, this relation is naturally not applicable to the measured waves in general. In reality the solitary waves are irregular and have a lot of deviation around their mean speed. Referring to Jurman

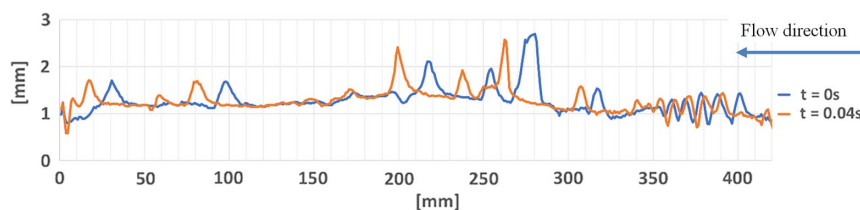


Fig. 10 Wave formations of de-icing fluid on the 0.6 m flat plate for an initial fluid thickness of 1.3 mm (wind tunnel speed 14.3 m/s).

and McCready [24] their analysis will not be capable of describing complete waveforms of solitary waves. If the solitary waves are transferring most of the fluid, their geometry in terms of amplitude and wave separation should also be known to estimate the relationship between the real mean wave speed and liquid film speed. However, according to the present study there appears to be a simple approximate relationship between the wave speeds and fluid flow-off rate—or liquid film mean velocity. This will be analyzed in detail below.

3. Fluid Flow-Off Rate Related to Wave Speeds

After preliminary filtering of the thickness signal the overall average thickness of the fluid was calculated by integrating the measured thickness values over the flat plate and dividing the result by the flat plate length. The wave speeds have been determined using two different methods. Especially at low speeds where periodical waves exist, autocorrelation function (MATLAB) of wave signal may be used. However, when analyzing the rapidly changing solitary waves the autocorrelation method becomes unreliable. To get reliable results, two adjacent wave curves with minimum time separation (0.02 s in 1.8 m model and 0.04 s in 0.6 m model) must be analyzed by the human eye to catch the wave movement and to calculate manually the individual wave speeds. In case of wave separation, a fast Fourier transform function was used. However, also the wave separation determination process needed manual verification.

Typical fluid thickness variations in time on a flat plate subjected to accelerated airstream are illustrated in Fig. 11. It shows one of the most documented fact of the fluid flow-off during the acceleration tests. The initial thickness does not affect the end thickness of the fluid after the test. This type of behavior applies to both de-icing and anti-icing (non-Newtonian) fluids and it has been indicated in several Refs. [3,4,21,22]. A comparison with the results of Cunha and Carbonaro [22] is included in Fig. 11. The wind tunnel of their study is the VKI CWT-1, referred to in the beginning of this section. Unfortunately, the viscosity of their de-icing fluid was not specified. The plate chords of these two tests are different. In the present study flat plate chord is 1.8 m, whereas the plate chord in study of Ref. [22] was 1.5 m.

The model scale effect on the relative fluid thickness variation is demonstrated in Fig. 12. The dimensionless thickness is expressed as percentage of the initial fluid thickness. As the absolute amount of fluid on the longer plate is threefold compared with the shorter plate, it is obvious that the relative thickness variation in accelerated airflow is delayed accordingly. This is examined in more detail below.

Considering the fluid flow-off from a plate of chord L that has a fluid layer of thickness h , we may deduce the mean fluid flow-off speed \bar{u} in two dimensions (Fig. 13) from the time variation of the

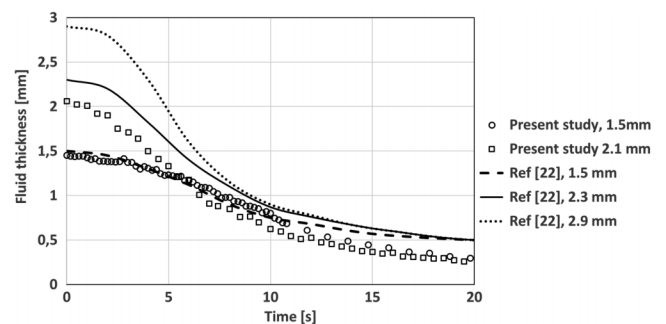


Fig. 11 Fluid thickness variation in time.

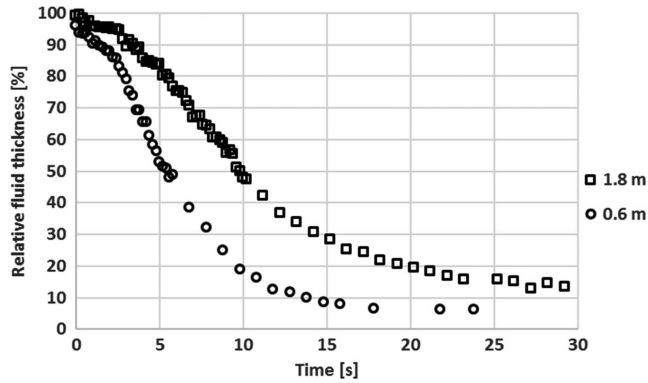


Fig. 12 Effect of the flat plate model chord on the variation of relative fluid thickness.



Fig. 13 Notations in a schematic model of a flat plate with a variable fluid layer on it.

thickness. For a unit width (span) of the plate, the volume difference in a time unit Δt is

$$-\Delta h L = \bar{u}(t)h(t)\Delta t \quad (2)$$

where $h(t)$ describes the thickness variation in time (dimensional version of Fig. 12), Δh is the reduction of thickness in time interval Δt , and $\bar{u}(t)$ is the instant mean flow of fluid through the cross section h . The mean flow velocity \bar{u} will then be

$$\bar{u} = -\frac{\Delta h}{\Delta t} \frac{L}{h(t)} \quad (3)$$

Figure 14 illustrates the mean flow velocity variation in time calculated from the data of dimensional thickness variation in time for both 0.6 and 1.8 m plates (as per Fig. 12) using Eq. (3).

Both curves in Fig. 14 have an almost linear region that seems to extend to the point where about 50% of the fluid on the plate has sheared off. This means the first 5 s for the 0.6 m plate and the first 10 s for 1.8 m plate (see Fig. 12). As the acceleration of the airspeeds is the same for both plates, this suggests that the mean fluid flow-off velocity depends linearly on the wind tunnel speed for the first 50% of fluid flow-off. In other words, the plate chord L does not affect the mean fluid flow-off speed \bar{u} . This will be considered in more detail below.

During the acceleration tests of the present study, periodic waves (Fig. 4) appear for a very short time (0.5–1 s). These waves are slow, and as they persist only for a short while, it is hard to find any relationship between air speed and wave speed. Once the solitary

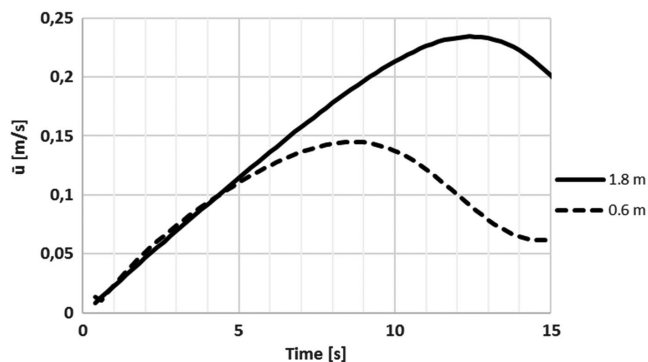


Fig. 14 Mean fluid film flow-off velocity variation in time during the acceleration test.

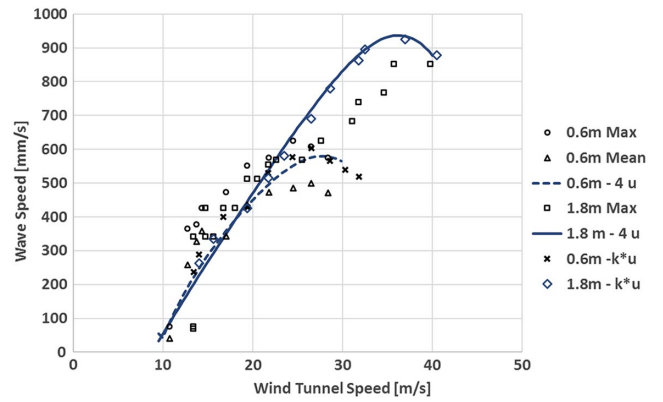


Fig. 15 Wave speed variation with wind tunnel speeds.

waves take over, the wave speeds multiply abruptly. Unlike the uniform periodic waves, the individual solitary waves move with different speeds, and typically faster waves take over the slower waves, merging with each other. However, considering the instant maximum and mean wave velocities, there is a clear relationship between the wave speeds and the wind tunnel speed as illustrated in Fig. 15. It is remarkable that the wave speeds for both plates follow approximately the same pattern once the statistical fluctuation is filtered out. This is observable up to the point where the wave speed slope begins to flatten out for the 0.6 m plate. For both plates (0.6 and 1.8 m) the almost linear relation to the wind tunnel speed flattens out at the point where the fluid layer has been reduced to about 40% of the initial thickness.

As pointed out in Sec. III.B. the thickness measurements include a general noise level of 0.2 mm. This in turn means that the wave speed observations become unreliable when the fluid layer thickness gets close to this value. The limit for reliable wave speeds is therefore lower for 0.6 m plate than for 1.8 m plate, where the fluid film thickness remains higher for a longer period. This explains the higher recorded wave speed data points for the 1.8 m plate compared with the 0.6 m plate in Fig. 15.

As already mentioned, according to the theoretical analysis of Jurman and McCready [24], the approximate wave speed is two times the mean fluid flow speed if the waves are considered to be kinematic in nature. This simplified relation between the wave speed and the fluid flow-off speed may not be generalizable for real kinematic waves. However, it is interesting in this context to compare the calculated fluid flow-off speed (Fig. 14) and the wave speeds. In Fig. 15 the mean flow-off speed multiplied by four ($c_w = 4\bar{u}$) is included for comparison with the wave speeds.

There is a clear reason for the factor of 4. If we assume that only the waves transfer the fluid, the ratio between wave speeds c_w and the mean fluid flow-off speed \bar{u} should reflect the volume fraction of waves compared with the total fluid volume on the plate. Thus, if the integrated wave volume is a quarter of the total fluid volume on the plate, the wave speed would then be four times \bar{u} . To find out the value of this factor, the wave volumes were integrated from the fluid surface curves (as in Fig. 10) and compared with the total volume of the fluid. The wave volume is defined here as the volume of the fluid above the envelope curve connecting the local minimums of the wave curve. The results are collected in Table 2. It is apparent that the factor four is an approximate value for the ratio between the mean wave speed c_w and the mean flow-off speed \bar{u} at a given wind tunnel speed U .

This suggests that there would be a simple approximate relationship between the wave speeds c_w and fluid flow-off speed \bar{u} though the ratio of these two is not necessarily four in general. In other words, waves are responsible for most of the fluid transfer. This in turn implies that the waves we are dealing with are kinematic waves in the sense of Jurman and McCready's analysis [24].

IV. Numerical Simulations

In the present study the computing resources for the numerical simulations consisted of a workstation computer with four CPU

Table 2 Factor k in the relation $c_w = k\bar{u}$, $c_w =$ wave speed, and $\bar{u} =$ mean flow-off speed

U , m/s	k
Plate chord 0.6 m	
13.7	4.59
14.3	4.38
14.3	4.53
17.0	4.28
19.4	4.12
21.8	4.33
24.5	4.23
26.5	4.23
28.4	3.91
30.4	3.78
31.8	3.84
34.6	3.90
Plate chord 1.8 m	
14.0	4.35
15.6	4.02
19.4	3.97
21.7	3.90
23.5	3.89
26.5	3.97
28.6	4.04
31.8	3.99
32.5	4.00
36.7	3.96
40.5	4.08
44.8	4.00
50.0	4.11

cores. This limited the level of ambition, and so the numerical simulations were carried out only for the 0.6 m flat plate model. Initial trials with a 1.8 m flat plate model turned out to be unacceptable, considering the time and resources available for the research.

A. Numerical Scheme

In the CFD simulation the mass conservation equations and the incompressible Navier–Stokes equations are numerically solved. The density ρ and the viscosity μ are determined in each cell by the volume fraction of the liquid and air that are present. The volume fraction of the liquid is denoted as α ; the density of the liquid and air are ρ_l and ρ_a , respectively. Then the density in a cell is $[\alpha\rho_l + (1 - \alpha)\rho_a]$, and similarly for μ . The equations for both phases were solved using the finite volume method, using the volume of fluid (VOF) method. This means that an advection equation is solved for the liquid volume fraction α .

Because the numerical solution of advection equations tends to produce numerical diffusion and thereby smear discontinuities, a special solution technique for the VOF equation is available in OpenFOAM. To guarantee a bounded solution with sharp interface between the phases, the flux-corrected transport approach MULTidimensional Limiter for Explicit Solutions (MULES) is used.

1. Solver

For the simulations the open source software library OpenFOAM, version 2.3.x, was used. As a solver the multiphaseInterFoam was selected. It is an incompressible solver for multiphase systems based on an Euler–Euler approach where all fluid phases are modeled as interpenetrating continuum—each of them according to Navier–Stokes equations with additional terms that account for the momentum exchange between the phases and interfacial forces. The main pressure–velocity coupling is done with PISO algorithm (Pressure-Implicit with Splitting of Operators) for the time-accurate simulation with three corrective (inner) iterations. This choice is conservative and yielded sufficient reduction in residual of the iterative pressure solution, which ensures mass conservation. On average, three orders of magnitude reduction were achieved.

Orthogonal corrections are not used, because the grid is fully orthogonal in the region of air–liquid interface. For the convection term $\nabla \cdot (\rho VV)$, the limited linear interpolation scheme (a second-order central differencing scheme with first-order upwind blending) was selected. All simulations were run with adaptive time stepping, keeping the maximum Courant number fixed at $CFL = v_i dt/dx_i = 0.85$, where v_i is the local velocity. In this way the time step was the same in all cells, determined by the most critical cell. Time steps were very short (e.g., 5×10^{-6} s). For this reason an Euler scheme was considered as sufficient to calculate the time derivatives $\delta/\delta t$.

2. Turbulence Treatment

When the de-icing fluid is spread over a surface, it forms a 1–2-mm-thick layer, which naturally becomes thinner at the leading and trailing edges. Therefore, the fluid layer is never subjected to a pure shear flow. Instead, the front of the fluid layer features some frontal area where pressure force initiates the first wave formation. Once this initial wave has formed at the front of the plate, the air flow separates at the wave crest, causing the flow downstream to become unsteady, dominated by vortex shedding. Thus, the relevance of considering a fully developed air flow over a liquid interface is practically lost. The test results above (Figs. 6 and 7) suggest that the de-icing fluid layer forms mostly 2D waves that travel across the surface, either merging with smaller and slower waves or ending up being absorbed by larger ones. Naturally there is some three-dimensionality as the waves seldom reach over the whole span of the model. This brings forth the following question: Are the 2D simulations able to capture this dynamic interaction between waves in reasonable accordance with experiments?

Some initial trials showed that no waves emerged on the surface when Reynolds-averaged Navier–Stokes modeling was used. The study of Thiruvengadam et al. [32] supports this finding. Although there is a general understanding that large eddy simulation (LES) and DNS modeling are fundamentally 3D simulation methods, there exist certain flow types in which the 2D LES modeling has been studied either as an initial or alternative method when faced with computer limitations.

In the literature the results of the simulation of two 2D vertical structures are contradictory. Bruno and Khris [33] and Bouris and Bergeles [34] claim the 2D LES to give reasonable results by optimizing the method or increasing the resolution near the wall [34], whereas Breuer [35] and Liefvendahl and Lillberg [36] consider 2D LES poor or even useless. Flows with reattaching separation bubbles have been studied with some success using 2D LES models. Wilson and Pauley [37] and Yu et al. [38] compare in their studies 2D and 3D LES models with experimental data. Both receive fairly good results also with 2D LES. A typical observation in comparisons between 2D and 3D LES models is that 2D computation can reveal only the properties of mean flow, but not fluctuating properties. In Yu et al. [39], only 2D LES is considered. Perhaps the most positive view of 2D LES is in density current and gravity current flow studies, where two stratified fluid layers with distinct densities have features common with two-phase fluids. Nourazar and Safavi [40] and Ooi et al. [41,42] compare 2D and 3D models and claim that a 2D model is able to capture most of the physics observed in experiments. There are also studies on free surface waves [43,44], where 2D LES have been used.

As noticed above, the gas phase in the two-phase flow problem incorporates unsteady vortex shedding. For this reason, an LES approach was used to capture as accurately as possible the air-stream-induced pressure and shear forces that transfer the liquid. The studies on successful application of 2D LES referred to above motivated further to select a 2D model to assess the possibilities to analyze the considered two-phase flow problem.

The basic concept of the LES method is to separate the velocity field to a resolved part and a subgrid part. The large eddies in the resolved part are solved explicitly, whereas the smaller eddies in the subgrid part are modeled using a subgrid scale (SGS) model. The separation of the velocity field is done using a filter width Δ , which is obtained from the computational grid. A Smagorinsky-type SGS model based on the local equilibrium assumption was used in all simulations. In the OpenFOAM implementation the eddy (SGS) viscosity is modeled according to the equation

$$\nu_{\text{sgs}} = C_k \sqrt{k} \Delta \quad (4)$$

The SGS viscosity equation is used everywhere in the computational domain. Here $C_k = 0.094$ and k is the kinetic energy of SGS turbulence. k is solved from an algebraic equation obtained by neglecting the transport terms (the whole left-hand side) of the modeled transport equation for k :

$$\frac{\partial k}{\partial t} + \frac{\partial}{\partial x_j} (\bar{u}_j k + d_j) = -\tau_{ij} \frac{\partial \bar{u}_{ii}}{\partial x_j} - \epsilon = P - \epsilon \quad (5)$$

where d_j contains the subgrid diffusive fluxes of k , and τ_{ij} is the subgrid stress tensor modeled as

$$\tau_{ij} = -\nu_{\text{sgs}} \left(\frac{\partial \bar{u}_i}{\partial x_j} + \frac{\partial \bar{u}_j}{\partial x_i} \right) + \frac{2}{3} k \delta_{ij} \quad (6)$$

where \bar{u}_i are the components of the resolved velocity field and δ_{ij} is the Kronecker delta.

The dissipation ϵ is modeled as

$$\epsilon = C_\epsilon k^{3/2} / \Delta \quad (7)$$

The dissipation coefficient C_ϵ is given the value 1.048.

The LES filter calculates the filter width Δ from the computational grid. A filter called cubeRootVolDelta in OpenFOAM was used. This is the cube root of the cell volume, but in 2D simulations the definition is the square root of the 2D area:

$$\Delta = \sqrt{V/dz} \quad (8)$$

where V is the volume of the cell, and dz is the grid width in the third dimension (plate span direction).

3. Computational Mesh and Boundary Conditions

Computational grid size was 160,000 cells. GridPro software was used for generating the 0.6 m × 0.5 m grid. The grid and the boundary conditions are illustrated in Fig. 16. The grid has a refined region spanning 60 mm from the flat plate surface. This refined region contains about half of the total cells. To simulate the eddies near the air–liquid interface, the grid was refined also in the horizontal direction close to the interface and wall. Insufficient resolution in Fig. 16 blurs cell faces to continuous white layers above the plate bottom surface and behind the air inlet surface. As there has to be a refinement in this area in both vertical and horizontal directions, quadrilateral cells were used instead of rectangular ones. These quadrilateral cells were orthogonal up to some 20 mm from the flat plate surface. Thereafter orthogonality reduces gradually upward to

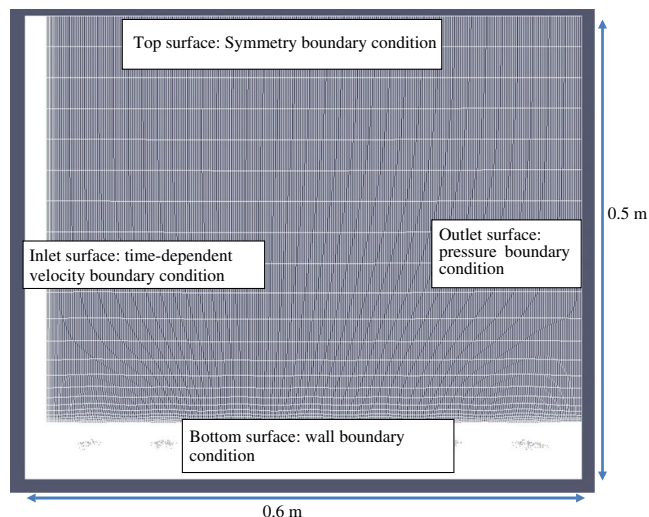


Fig. 16 Computational grid (0.6 m × 0.5 m) and boundary conditions.

coarse the grid far away from the surface in order to save the total amount of cells.

Typical cell size in the fluid interface is about 0.5 mm × 0.1 mm (length × height) and at the flat plate surface 0.5 mm × 0.0125 mm ($y^+ = 0.75$). For the air–fluid interface, the conventional friction-velocity-based nondimensional wall distance y^+ may not be a relevant criterion for two reasons. As the airflow over the waves consists of separated flow regions, the shear stresses are often near zero or negative. Also, the pressure forces are the principal driving mechanisms for the solitary waves, whereas friction forces are far less important. The grid resolution criterion at the liquid–gas interface is dictated by the wave dynamics—the liquid interface needs to capture the evolution of the solitary waves with sufficient detail. The grid was refined until further refinement yielded no observable effect in the wave dynamics.

A grid convergence study was carried out with a grid size of 400,000 cells. The grid refinement concentrated to the vicinity of the flat plate surface. The refined grid improved somewhat the results. However, this was accomplished with a cost of more than fivefold increase in computing time.

The gas flow undergoes perpetual fluctuations, forming vortices at the front of the liquid layer. These vortices are convected downstream over the liquid interface. On a flat plate with a chord of 0.6 m and airspeed 10 m/s, the lifetime of a fluid particle in the domain is roughly 0.06 s. We can consider this as a global time scale for the gas-phase vortices. The highly viscous liquids have barely formed a single wave at the front part of the liquid layer within 0.5 s after the gaseous fluid particle entered the domain. This indicates that the global time scale of the waves can reasonably be expected to be two orders of magnitude larger than that of the air particles. This is problematic as the numerical requirements of the CFD simulation are dictated by the vortex-shedding-dominated gas-phase physics as well as the interface behavior. These demand a relatively high grid resolution particularly at the interface and sufficiently short time steps to capture the flow system’s behavior adequately. A typical time step is roughly 5×10^{-6} s, which unavoidably leads to long computational times. The simulation times were mostly 10 s.

In the boundary conditions illustrated in Fig. 16 the outlet surface pressure boundary condition is a zero-pressure difference condition. For the phase fraction α the variableHeightFlowRate boundary condition was selected to enable a free liquid exit at the trailing edge.

B. Results and Evaluation

In experimental studies the wind tunnel speed was accelerated from an “idle speed” of approximately 5 m/s up to 60 m/s. In the numerical simulation the initial inflow speed of the air was chosen to be 2 m/s to facilitate subtle initial conditions and a stable start for computation. Otherwise the time dependency (acceleration) of the inflow speed followed closely the wind tunnel speed sequence. To avoid excessive computation time the simulation time was limited to 10 s, which implies a maximum air inlet speed of 29.1 m/s. Except for some initial tests the fluid layer was selected to be 1 mm in all numerical simulations to match closely the fluid layer thicknesses in the wind tunnel tests.

1. General Observations on the Airflow

As long as the fluid layer surface remains nearly flat, the air velocity distribution resembles a typical boundary-layer type of distribution in the vertical direction. Once the first waves build up, flow separation appears on the leeward side of the waves. Sequential flow separations will in turn generate downstream moving vortices—see Fig. 17. When the number of waves increases and all individual waves generate downstream vortices, the air layer above the fluid surface will be covered by a vortex street as illustrated in Fig. 18. The air pressure fluctuates due to the vortex street generated by the waves as described in Fig. 19. In Fig. 19 the ambient pressure is set to zero and the color coded scale figures are pressure differences from ambient pressure in Pa. In Figs. 17–19, the x and y directions are in scale 1 : 1.

According to the classical wind wave theories of Phillips [11] and Miles [12] the pressure fluctuations have a significant role in the

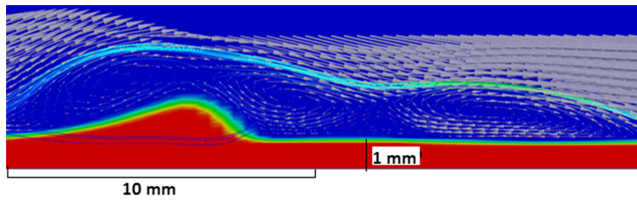


Fig. 17 Flow separation at the crest of the wave and the following downstream vortex.

transfer mechanism of a wavy liquid. However, the exact assessment of the contribution of pressure and friction forces for fluid transfer is considered to be beyond the scope of this paper.

2. Wave Onset

In the experiments the first waves appearing at airspeeds of 8.5–10 m/s were periodic (Figs. 4 and 6). These periodic waves spread over the whole liquid surface within 1 s. As the airspeed was accelerated, the periodic waves were replaced gradually by solitary waves so that the first solitary waves at the leading-edge area formed already, whereas the periodic waves still were spreading along the plate area.

In the numerical simulation the onset of periodic waves does not appear. The waves that initially appear on the fluid film over the flat plate are irregular solitary waves as illustrated in Fig. 20. Some initial tests with inflow airspeeds up to 18 m/s were done with computational grid size of 400,000 and refined numerical discretization schemes. However, no signs of initial periodic waves were discovered. The reason for this remains unclear. There are no studies known by the authors where the periodic waves would have been detected using CFD methods in a corresponding two-phase problem. Saka-keeney et al. [29] investigated water film behavior on a NACA 0012 wing section surface using both 2D and 3D DNS. The waves their simulation generates on the water surface are not defined according to their periodicity. However, according to the figures in [29] the liquid layer waves seem irregular in amplitude and hence solitary in nature.

3. Kinematic and Dynamic Waves

Although the sequence of events during the measured wave onset was not exactly replicated in the computational results, there were signs of isolated areas with periodic waves among the solitary waves. They seem to appear immediately behind the solitary waves, which may suggest that air stream disturbances induce the periodic waves. The inlet air velocity at the front edge of calculation domain was accelerating in steady manner and was never tested with added disturbances.

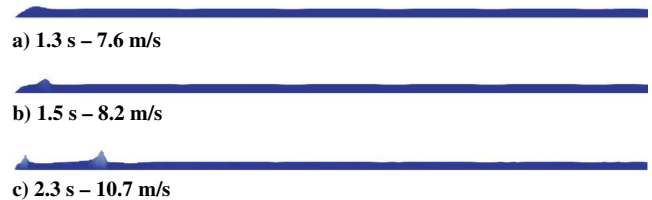


Fig. 20 Calculated initial wave formation on the 0.6 m plate for three sequential points of time and inlet air speed.

When considering the calculated fluid motion on the plate, it seems obvious that the solitary waves are responsible for most of the fluid transfer. This is illustrated in Fig. 21, where the x -direction velocity of the fluid layer is color coded. The wave front illustrated in Fig. 21 includes slower periodic waves too. The dynamic standing waves are located between $x = 0.5$ and 0.6 m. Part of the figure is magnified to clarify the difference in fluid velocity in a wave compared with the fluid velocity between the waves.

The fluid transfer aspect is further emphasized in Fig. 22, where the fluid momentum is color coded. The solitary waves are clearly responsible for the fluid mass flow. The illustrated division into the waves that transfer the fluid and those that do not is well in line with what Jurman and McCready [24] concluded with in their analysis of kinematic and dynamic waves.

4. Fluid Flow-Off Rate, Wave Speeds, and Wave Geometry

As reasoned above, the fluid transfer is carried out almost totally by the solitary waves on the plate. Considering the computational simulation of the fluid flow-off rate, the most essential parameters are wave speed and wave geometry, which in this respect consists mainly of wave amplitude and separation. Although the wave form naturally affects the fluid amount transferred, the waves are observed to be similar on all scales with a reasonable accuracy. This applies to both measurements and computational simulations. Next the success of the numerical simulation in the fluid flow-off rate is evaluated considering the parameters affecting it.

Figure 23 illustrates the measured and the CFD-simulated relative fluid thickness variation in time during the acceleration test. The simulation time span is 10 s. Note that here the time frame is different from the one in Fig. 12, and as in Fig. 23 the time axis has been selected to get the wind tunnel speed and simulated air inlet speed to match. The air inlet speed to the simulation domain and the wind tunnel speed are included in the figure. Obviously, the fluid begins to deplete in the tests 2.5 s before the corresponding event in the CFD simulation. However, the calculated thickness values merge with the measured values within 6 s from the start as the wind tunnel speed is

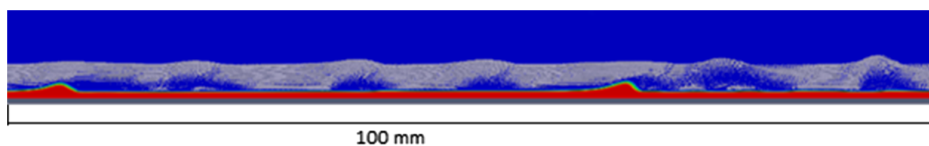


Fig. 18 Vortex shedding of airflow (white arrows are airspeed vectors) over a wavy liquid surface (red surface).

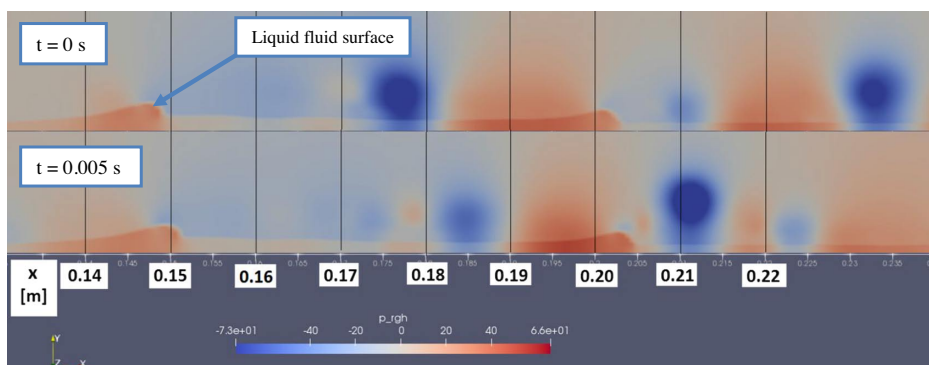


Fig. 19 Pressure fluctuation variation in time above the fluid surface.

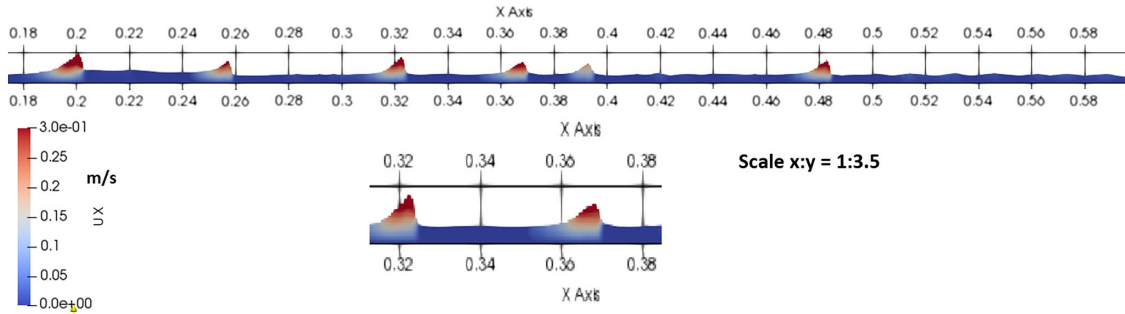


Fig. 21 Fluid horizontal velocity on the 0.6 m flat plate with wind tunnel speed of 15.3 m/s indicated in color codes.

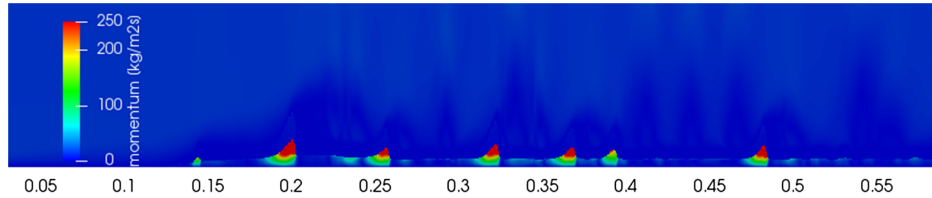


Fig. 22 Fluid momentum color coded [kg/(m² · s)]. x-y coordinates scaled 1 : 5. Inlet air speed is 15.3 m/s.

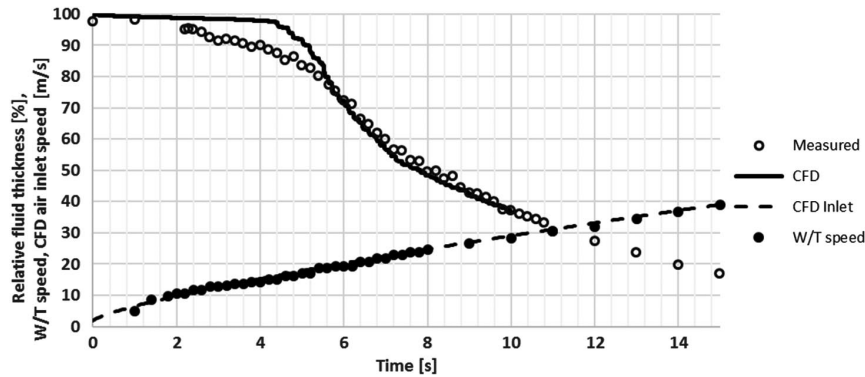


Fig. 23 Fluid relative thickness variation in time on the 0.6 m plate during the acceleration test. Measurements compared with CFD simulation results.

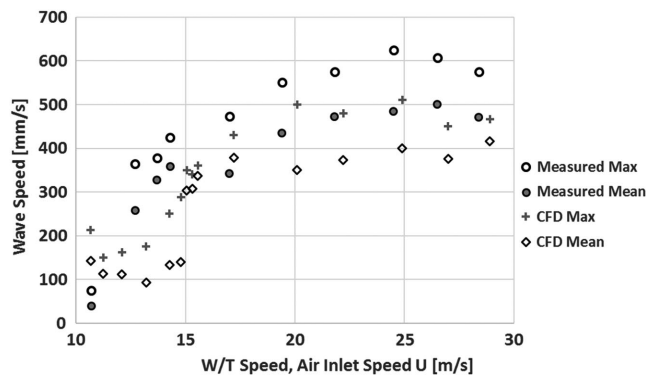


Fig. 24 Measured and calculated wave speed variation with wind tunnel speed and air inlet speed (CFD) for the 0.6 m plate.

20 m/s. From there on, the calculated values follow closely the measured ones. The air inlet speed at the end of simulation is 29.1 m/s.

Figure 24 illustrates the measured and CFD simulated fluid wave speeds on the 0.6 m flat plate during the acceleration test. Both maximum and mean wave speed values are included. The measured values are two to three times higher than the calculated ones once the solitary waves appear (wind tunnel speed or simulated air inlet speed > 10 m/s). This discrepancy continues approximately to a wind tunnel speed (air inlet speed) of 15 m/s. Thereafter the trends of calculated and measured values are similar though the calculated values

are clearly (20–30%) lower than the measured values. In Fig. 23 the point where the wind tunnel speed reaches 15 m/s corresponds to the point where the calculated fluid relative thickness begins to decrease more clearly to catch the measured values. This relationship between wave speeds and fluid transfer rate is in line with the characteristics of kinematic waves referred to above.

There is a clear jump in calculated (CFD) mean wave speeds around the simulated inlet speed of 15 m/s that needs to be explained. Up to the point of inlet speed 15 m/s the simulated wave formation differs from the real observed one remarkably. At simulation time 2.6 s (inlet flow speed of 11.5 m/s) a bulge of fluid builds up on the leading-edge area of the plate. This bulge persists up to simulation time of 3.4 s (13.7 m/s) and feeds waves one by one further downstream the plate. The waves are very slow at the bulge area, and only the detached waves speed up. During this period the plate contains very few waves, and they concentrate on the leading-edge area. This explains why the mean values differ so clearly from the maximum values, as the slow waves dominate the statistics. During simulation times from 3.5 to 4.0 s (14–15.3 m/s) the things change abruptly as the number of waves increases suddenly from 4 to 14. This will increase the mean value clearly closer to the maximum values. When the inlet speed increases further, the difference between wave speed mean values and maximum values follows approximately the same pattern as for measured values.

Assuming the obvious correlation between the flow rate and the wave speeds on the fluid layer, it is apparent that also the geometry [wave amplitude and separation (Fig. 7)] influences the flow rate. The measured and CFD-simulated values of relative amplitude a/h and wave separation S are illustrated in Figs. 25 and 26. The relative

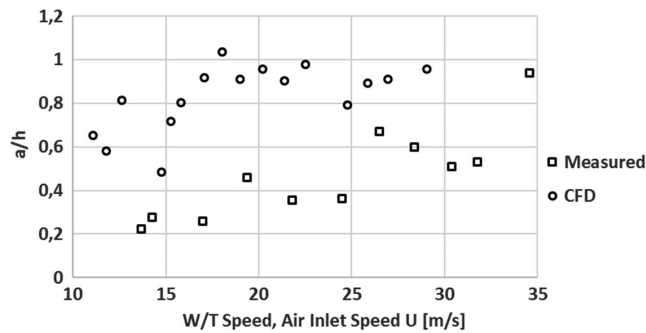


Fig. 25 Measured and calculated relative amplitude a/h for the 0.6 m plate.

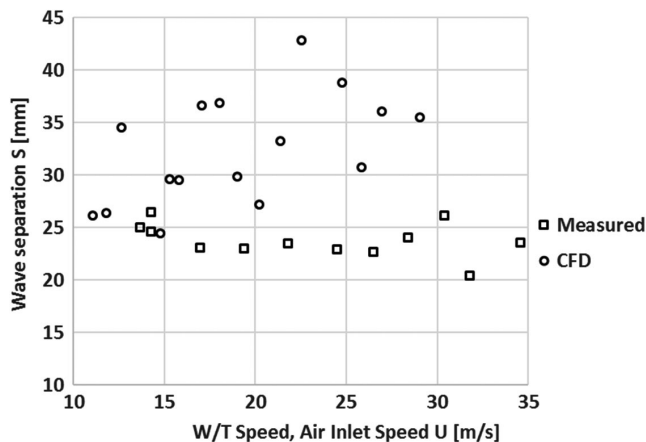


Fig. 26 Measured and calculated mean wave separation for the 0.6 m flat plate.

amplitude a/h seems to be dependent on the wind tunnel speed, whereas the wave separation does not show any such correlation. The calculated values of both relative amplitude a/h and of wave separation S are clearly higher than the measured ones.

If the assumption that the kinematic waves are responsible for fluid transfer is accepted, the mean fluid flow-off speed is proportional to the absolute amplitude a and the wave speed c_w , and inversely proportional to the wave separation:

$$\bar{u} \sim \frac{a}{S} c_w \quad (9)$$

Considering the relative amplitude, the thickness of the fluid, and the wave speed from the point when the wind tunnel speed has reached 20 m/s, there is approximately a 30% difference between calculated and measured mean values of amplitude to separation ratio (a/S). This compensates the difference in calculated and measured wave speed values (–20 to –30%), which in turn may explain the satisfactory results for the CFD-simulated relative thickness variation in time once wind tunnel speed has reached 20 m/s.

As stated earlier some improvements in the results were accomplished by refining the grid. For the tested simulation time of 5 s, wave amplitudes and separations came closer to the measured values. Also, the mean thickness curve followed the measured one better from the start of the simulation. However, the cost of this was more than fivefold increase in computing time.

V. Conclusions

This study was motivated by the obvious lack of understanding on the mechanism of fluid film flow-off from a flat plate subjected to an accelerating airstream. The previous studies on the subject have focused mainly on the stability issues of two-phase flows. That kind of approach never reveals the mechanics of mass transfer but gives only conditions for the first periodic wave onset and the possibility to estimate the characteristics of these periodic waves. It is, however, the

solitary waves that transfer fluid in the two-phase flow situation described.

The present study is divided into experiments with two flat plates with different chords (0.6 and 1.8 m) and CFD simulations for the shorter flat plate model. Experiments consist of wind tunnel tests for flat plates that are applied with type I de-icing fluid. The fluid thickness distribution is measured in time using the light absorption technique. The fluid film thickness measurement accuracy and resolution were estimated to be approximately 0.2 mm. However, as the main cause for the limited resolution was the relatively high evenly distributed noise level of measurements, this did not affect the integrated mean fluid thickness variation in time, which played an important role in the study. The limited measurement resolution did not affect the analysis of wave phenomena either, as the most important waves were clearly higher than 0.2 mm. The wave speed resolution was estimated to be 0.04 mm/s, which was well enough to measure wave speeds ranging from 40 to 900 mm/s.

The periodic wave onset and characteristics of first periodic waves are in line with the scarce results from previous studies with similar fluids. One of the objectives was to identify the solitary waves on the plates as so-called kinematic waves. The interconnection between the measured fluid flow-off and solitary wave speeds suggests that solitary waves are kinematic in the sense referred to by Jurman and McCready [24]. This means that the solitary waves are responsible for the fluid mass transfer. According to measurements the wave speeds and the mean 2D fluid flow-off speed (m/s) are almost linearly dependent on the wind tunnel speed down to 50% of initial fluid film thickness. From there on, the wave speeds and the mean fluid flow-off speeds follow identical patterns up to the point where waves become incoherent and measured wave speeds unreliable. This suggests that, as far as the waves are measurable, they are kinematic in nature and responsible for fluid mass transfer.

The CFD simulations were done using OpenFOAM software library employing LES-type approach. As the vortex shedding from the waves was assumed to dominate the airflow, an LES-type turbulence treatment was selected.

The results showed that the air flow was dominated by vortex shedding as expected, which suggested that the forces directed to the liquid fluid were irregular and fluctuating. The simulated fluid flow supported clearly the assumption of kinematic waves. According to calculated results the waves are practically completely responsible for the fluid mass transfer.

The calculations of fluid thickness variation in time reproduced the observations only partly well as the modeled flow-off was clearly delayed for the first 4–5 s from the measured values. However, toward the end of calculation time (10 s) the calculated values merged with the measured values. The reason for the initial discrepancy between the measured and calculated flow-off rates was that the calculated wave speed values at the lowest wind tunnel (inlet) speeds (<15 m/s) were too low. The calculated wave amplitudes and separations were both overestimated by approximately 30%. However, these errors compensated each other in the calculated fluid flow-off rate.

Acknowledgments

This work was supported jointly by U.S. Federal Aviation Administration and the Finnish Transport Safety Agency. The wind tunnel models were designed and manufactured by Juha Kivekäs, Arteform, Ltd.

References

- [1] "Standard Test Method for Aerodynamic Acceptance of SAE AMS 1424 and SAE AMS 1428 Aircraft Deicing/Anti-Icing Fluids," SAE International, AS5900 Rev. C, Warrendale, Pennsylvania, Oct. 2016. <https://doi.org/10.4271/AS5900C>
- [2] Hill, E. G., and Zierten, T. A., "Aerodynamic Effects of Aircraft Ground Deicing/Anti-Icing Fluids," *Journal of Aircraft*, Vol. 30, No. 1, Jan.–Feb. 1993, pp. 24–34. <https://doi.org/10.2514/3.46301>
- [3] Hill, E. G., "Aerodynamic Acceptance Test for Aircraft Ground Deicing/Anti-Icing Fluids," Boeing Doc. D6-55573, Boeing Co., Seattle, WA, Oct. 1990.

- [4] Runyan, L. J., Zierten, T. A., Hill, E. G., and Addy, H. E., "Lewis Icing Research Tunnel Test of the Aerodynamic Effects of Aircraft Ground Deicing/Anti-Icing Fluids," NASA TP 3238, Aug. 1992.
- [5] Hendrickson, G. S., and Hill, E. G., *Effects of Aircraft De-/Anti-Icing Fluids on Airfoil Characteristics*, Influence of Environmental Factors on Aircraft Performance, von Karman Inst. for Fluid Dynamics, Brussels, Feb. 1987.
- [6] Carbonaro, M., "Experimental Study of the Flow of a Film of Aircraft Deicing Fluid During a Simulated Take Off at Subfreezing Temperature," von Karman Inst. for Fluid Dynamics CR1985-02, Brussels, May 1985.
- [7] Carbonaro, M., "Experimental Study of the Aerodynamic Characteristics of a Two-Dimensional Wing Model Covered with De/Anti-Icing Fluid During a Simulated Take Off at Subfreezing Temperature," von Karman Inst. for Fluid Dynamics CR 1986-22, Brussels, Aug. 1986.
- [8] Carbonaro, M., "Further Study of the Aerodynamic Performance of a 2-D Wing Model Covered with Simulated Frost or with De/Anti Icing Fluid During a Simulated Take Off at Subfreezing Temperature," von Karman Inst. for Fluid Dynamics CR1987-29, Brussels, July 1987.
- [9] Thomson, W., "On the Waves Produced by a Single Impulse in Water of Any Depth, or in a Dispersive Medium," *Proceedings of the Royal Society London*, Vol. 42, Nos. 251–257, 1887, pp. 80–83.
- [10] von Helmholtz, H. L., "On Discontinuous Movements of Fluids," *Philosophical Magazine*, Vol. 36, No. 244, 1868, pp. 337–346.
- [11] Phillips, O. M., "On the Generation of Waves by Turbulent Wind," *Journal of Fluid Mechanics*, Vol. 2, No. 5, 1957, pp. 417–445. <https://doi.org/10.1017/S0022112057000233>
- [12] Miles, J. W., "On the Generation of Surface Waves by Shear Flows," *Journal of Fluid Mechanics*, Vol. 3, No. 2, 1957, pp. 185–204. <https://doi.org/10.1017/S0022112057000567>
- [13] Cohen, L. S., and Hanratty, T. J., "Generation of Waves in Concurrent Flow of Air and a Liquid," *AIChE Journal*, Vol. 11, No. 1, 1965, pp. 138–144. [https://doi.org/10.1002/\(ISSN\)1547-5905](https://doi.org/10.1002/(ISSN)1547-5905)
- [14] Craik, A. D. D., "Wind-Generated Waves in Thin Liquid Films," *Journal of Fluid Mechanics*, Vol. 26, No. 2, 1966, pp. 369–392. <https://doi.org/10.1017/S0022112066001289>
- [15] Yih, C. S., "Wave Formation on a Liquid Layer for Deicing Airplane Wings," *Journal of Fluid Mechanics*, Vol. 212, No. 1, 1990, p. 41. <https://doi.org/10.1017/S0022112090001847>
- [16] Miesen, R., and Boersma, B. J., "Hydrodynamic Stability of a Sheared Liquid Film," *Journal of Fluid Mechanics*, Vol. 301, Oct. 1995, pp. 175–202. <https://doi.org/10.1017/S0022112095003855>
- [17] Boelens, O. J., Moeleker, P. J. I., deJong, H., and Hoefmakers, H. W. M., "Numerical Methods For Simulating the Flow over an Airfoil, Covered with a Thin Layer of Liquid," Paper ICAS-96-1.4.3, International Council of the Aeronautical Sciences, Bonn, Germany, 1996.
- [18] Tsao, J.-C., Rothmayer, A. P., and Ruban, A. I., "Stability of Airflow Past Thin Liquid Films on Airfoils," *Computers and Fluids*, Vol. 26, No. 5, 1997, pp. 427–452. [https://doi.org/10.1016/S0045-7930\(97\)00005-4](https://doi.org/10.1016/S0045-7930(97)00005-4)
- [19] Boelens, O. J., and Sijp, J. C., "Investigation into the Formation of Waves on Thin Layers of De/Anti-Icing Fluids on Wings," Paper ICAS-A98-31718, International Council of the Aeronautical Sciences, Bonn, Germany, 1998.
- [20] Özgen, S., Degrez, G., and Sarma, G. S. R., "Two-Fluid Boundary Layer Stability," *Physics of Fluids*, Vol. 10, No. 11, 1998, pp. 2746–2757. <https://doi.org/10.1063/1.869798>
- [21] Carbonaro, M., and Özgen, S., "Aerodynamic Effects of De/Anti-Icing Fluids and a Description and Test Techniques for their Aerodynamic Acceptance," Ice Accretion Simulation, Advisory Group for Aerospace and Development Rept. AR-344, 1997.
- [22] Cunha, F., and Carbonaro, M., "Surface Wave Instability on Aircraft De/Anti-Icing Fluid Films," *First European Symposium: The Mechanics of Film Coating*, World Scientific Publ., Singapore, 1995.
- [23] Özgen, S., Carbonaro, M., and Sarma, G. S. R., "Experimental Study of Wave Characteristics on a Thin Layer of De/Anti-Icing Fluid," *Physics of Fluids*, Vol. 14, No. 10, Oct. 2002, pp. 3391–3402. <https://doi.org/10.1063/1.1501282>
- [24] Jurman, L. A., and McCready, M. J., "Study of Waves on Thin Liquid Films Sheared by a Turbulent Gas Flow," *Physics of Fluids A*, Vol. 1, No. 3, March 1989, pp. 522–536. <https://doi.org/10.1063/1.857553>
- [25] Peng, C.-A., Jurman, L. A., and McCready, M. J., "Formation of Solitary Waves on Gas Sheared Liquid Layers," *International Journal of Multi-phase Flow*, Vol. 17, No. 6, 1991, pp. 767–782. [https://doi.org/10.1016/0301-9322\(91\)90055-8](https://doi.org/10.1016/0301-9322(91)90055-8)
- [26] Vlachomitrou, M., and Pelekasis, N., "Short to Long Wave Resonance and Soliton Formation in Boundary Layer Interaction with a Liquid Film," *Journal of Fluid Mechanics*, Vol. 660, Oct. 2010, pp. 162–196. <https://doi.org/10.1017/S0022112010002612>
- [27] Leng, M., Chang, S., Lian, Y., and Wu, H., "Experimental Study of Water Film Dynamics Under Wind Shear and Gravity," *AIAA Journal*, Vol. 56, No. 5, 2018, pp. 1803–1811. <https://doi.org/10.2514/1.J056440>
- [28] Leng, M., Chang, S., and Wu, H., "Experimental Investigation of Shear-Driven Water Film Flows on Horizontal Metal Plate," *Experimental Thermal and Fluid Science*, Vol. 94, June 2018, pp. 134–147. <https://doi.org/10.1016/j.expthermflusci.2018.02.004>
- [29] Sakakeeny, J. A., McClain, S. A., and Ling, Y., "Direct Numerical Simulation of a Thin Film over a NACA 0012 Airfoil," *2018 Atmospheric and Space Environments Conference, AIAA AVIATION Forum*, AIAA Paper 2018-2857, 2018. <https://doi.org/10.2514/6.2018-2857>
- [30] Craik, A. D. D., Latham, R. C., Fawkes, M. J., and Gribbon, P. W. F., "The Circular Hydraulic Jump," *Journal of Fluid Mechanics*, Vol. 112, No. 1, 1981, p. 347. <https://doi.org/10.1017/S002211208100044X>
- [31] Lighthill, M. J., and Whitham, G. B., "On Kinematic Waves I. Flood Movement in Long Rivers," *Proceedings of the Royal Society of London. Series A*, Vol. 229, No. 1178, 1955, pp. 281–316. <https://doi.org/10.1098/rspa.1955.0088>
- [32] Thiruvengadam, M., Armary, B. F., and Drallmeier, J. A., "Shear-Driven Liquid Film in a Duct," *Engineering Applications of Computational Fluid Mechanics*, Vol. 3, No. 4, 2009, pp. 506–513. <https://doi.org/10.1080/19942060.2009.11015287>
- [33] Bruno, L., and Khris, S., "The Validity of 2D Numerical Simulations of Vertical Structures Around a Bridge Deck," *Mathematical and Computer Modelling*, Vol. 37, No. 8, 2003, pp. 795–828. [https://doi.org/10.1016/S0895-7177\(03\)00087-6](https://doi.org/10.1016/S0895-7177(03)00087-6)
- [34] Bouris, D., and Bergeles, G., "2D LES of Vortex Shedding from a Square Cylinder," *Journal of Wind Engineering and Industrial Aerodynamics*, Vol. 80, Nos. 1–2, 1999, pp. 31–46. [https://doi.org/10.1016/S0167-6105\(98\)00200-1](https://doi.org/10.1016/S0167-6105(98)00200-1)
- [35] Breuer, M., "Large Eddy Simulation of the Subcritical Flow Past a Circular Cylinder: Numerical and Modeling Aspects," *International Journal for Numerical Methods in Fluids*, Vol. 28, No. 9, 1998, pp. 1281–1302. [https://doi.org/10.1002/\(ISSN\)1097-0363](https://doi.org/10.1002/(ISSN)1097-0363)
- [36] Liefvendahl, M., and Lillberg, E., "Computational Methods for Unsteady Fluid Force Predictions Using Moving Mesh Large Eddy Simulations," AIAA Paper 2005-4144, 2005.
- [37] Wilson, P. G., and Pauley, L. L., "Two- and Three-Dimensional Large-Eddy Simulations of a Transitional Separation Bubble," *Physics of Fluids*, Vol. 10, No. 11, 1998, pp. 2932–2940. <https://doi.org/10.1063/1.869813>
- [38] Yu, K. F., Lau, K. S., Chan, C. K., and Zhang, H. Q., "2D and 3D Computation for Two Phase Flow by Large Eddy Simulation and a Lagrangian Model," *Proceedings of the 3rd IASME/WEAS International Conference on Fluid Dynamics and Aerodynamics*, Aug. 2005, pp. 267–272.
- [39] Yu, K. F., Lau, K. S., and Chan, C. K., "Numerical Simulation of Gas-Particle Flow in a Single-Side Backward-Facing Step Flow," *Journal of Computational and Applied Mathematics*, Vol. 163, No. 1, Feb. 2004, pp. 319–331. <https://doi.org/10.1016/j.cam.2003.08.077>
- [40] Nourazar, S., and Safavi, M., "Two-Dimensional Large-Eddy Simulation of Density-Current Flow Propagating up a Slope," *Journal of Hydraulic Engineering*, Vol. 143, No. 9, Sept. 2017, Paper 04017035. [https://doi.org/10.1061/\(ASCE\)HY.1943-7900.0001329](https://doi.org/10.1061/(ASCE)HY.1943-7900.0001329)
- [41] Ooi, S. K., Constantinescu, G., and Weber, L. J., "2D Large-Eddy Simulation of Lock-Exchange Gravity Current Flows at High Grashof Numbers," *Journal of Hydraulic Engineering*, Vol. 133, No. 9, 2007, pp. 1037–1047. [https://doi.org/10.1061/\(ASCE\)0733-9429\(2007\)133:9\(1037\)](https://doi.org/10.1061/(ASCE)0733-9429(2007)133:9(1037))
- [42] Ooi, S. K., Constantinescu, G., and Weber, L., "Numerical Simulations of Lock-Exchange Compositional Gravity Current," *Journal of Fluid Mechanics*, Vol. 635, No. 1, 2009, pp. 361–388. <https://doi.org/10.1017/S0022112009007599>
- [43] Yang, J., and Stern, F., "Large-Eddy Simulation of Breaking Waves Using Embedded-Boundary/Level-Set Method," AIAA Paper 2007-1455, 2007.
- [44] Lu, X., Zou, Q., and Reeve, D. E., "2D Large-Eddy Simulation of Water-Wave Impact During Violent Overtopping Events," *Coastal Engineering Proceedings*, Vol. 1, No. 32, Feb. 2011, p. structures.16. <https://doi.org/10.9753/icce.v32.structures.16>